Acta Materialia 309 (2026) 122134

Contents lists available at ScienceDirect

Acta Materialia

journal homepage: www.elsevier.com/locate/actamat

Full length article

Compositional softening and non-basal slip in off-stoichiometric Ca–Mg–Al *C*14 Laves phases

Martina Freund *, Sang-Hyeok Lee, Peter Koch, Pei-Ling Sun, Zhuocheng Xie, Sandra Korte-Kerzel

Institute of Physical Metallurgy and Materials Physics, RWTH Aachen University, Germany

ARTICLE INFO

Keywords:
Laves phase plasticity
Off-stoichiometry
Electron microscopy
Nanoindentation
Atomistic simulation

ABSTRACT

The effect of off-stoichiometric alloying on the mechanical behaviour of the hexagonal *C*14 Ca-Mg-Al Laves phase was investigated through a combined atomistic modelling and experimental approach. Atomistic simulations were used to explore the compositional space and characterise the resulting transitions in elastic and plastic properties. The calculations reveal that partial substitution of Mg by Ca significantly reduces elastic stiffness and unstable stacking fault energies, indicating enhanced dislocation mobility in Ca enriched compositions. A ternary *C*14 $Ca_{37}Mg_{61}Al_2$ phase was synthesised and analysed to validate these predictions. Nanoindentation yielded an average hardness of 2.4 ± 0.3 GPa and modulus of 50.0 ± 1.9 GPa, representing a ~32 % hardness reduction relative to binary $Ca_{31}Mg_{69}$. Slip trace analy-sis and transmission electron microscopy confirmed dominant non-basal deformation involving prismatic and pyramidal ⟨*a*⟩ dislocations, as well as the occurrence of cross-slip. The agreement between simulations and experiments demonstrates that the enrichment with larger Ca atoms induces lattice dilation and facilitates dislocation activity. This compositional softening mechanism provides a route to tune the plasticity of Laves phases through controlled off-stoichiometric alloying.

1. Introduction

Laves phases represent one of the most important families of intermetallic compounds, not only because of their abundance and significance in functional applications such as hydrogen storage, magnetism, and superconductivity, but also due to their role in structural alloys [1]. In Mg–Al systems, strengthening is commonly attributed to the formation of the β-$Mg_{17}Al_{12}$ phase [2–4]. While this phase contributes to precipitation hardening at ambient and moderately elevated temperatures, it undergoes rapid coarsening and loses coherency with the Mg matrix above ~120–200 °C, and may dissolve entirely at higher treatment temperatures, thereby limiting the applicability of Mg–Al alloys under high-temperature service conditions [3,4]. The addition of Ca fundamentally alters this behaviour: Ca promotes the formation of thermally more stable intermetallics, $CaMg_2$, $CaAl_2$ and $Ca(Mg,Al)_2$ Laves phases (*C*14, *C*15, and *C*36 types), while suppressing or replacing $Mg_{17}Al_{12}$ [5,6]. These Ca containing Laves phases are more resistant to coarsening than β-$Mg_{17}Al_{12}$, remain effective as strengthening constituents at elevated temperatures, and further improve creep resistance, corrosion performance, and oxidation resistance [7]. Beyond their technical benefits, Ca is also an abundant and low-cost alloying element, making the Mg–Al–Ca system a particularly promising pathway for developing lightweight structural materials with enhanced high-temperature stability [8–12]. Nevertheless, despite their technological potential, Laves phases are macroscopically brittle at ambient temperatures and exhibit complex, not yet fully understood deformation mechanisms. While their presence in Mg–Al–Ca alloys can clearly contribute to strengthening, corrosion resistance, and high-temperature stability, the fundamental behaviour of the Laves phases themselves remains only partially characterised. A comprehensive understanding of their intrinsic mechanical response is, however, essential, since the beneficial effects in real alloys ultimately arise from their interaction with the surrounding Mg matrix. This challenge becomes even more pronounced when moving beyond strictly binary model systems, as is unavoidable in practical alloys where Laves phases typically form with local chemical fluctuations or ternary substitutions.

Laves phases are members of the topologically close-packed (TCP) family and typically exhibit brittle behaviour at room temperature, with a brittle-to-ductile transition temperature (BDTT) near 0.6 T_H, where T_H represents the homologous temperature [13–17]. Binary Laves phases

* Corresponding author at: Dr.-ing Institute of Physical Metallurgy and Materials Physics Aachen, NRW Germany.
E-mail address: freund@imm.rwth-aachen.de (M. Freund).

https://doi.org/10.1016/j.actamat.2026.122134
Received 1 December 2025; Received in revised form 13 March 2026; Accepted 15 March 2026
Available online 16 March 2026
1359-6454/© 2026 The Authors. Published by Elsevier Inc. on behalf of Acta Materialia Inc. This is an open access article under the CC BY license (http://creativecommons.org/licenses/by/4.0/).

are often characterised by a narrow homogeneity range around their stoichiometric composition AB_2, which can differ regarding their prototype structure. Ideal solubility is reported for these phases with an atomic radius ratio of the A and B atoms of $\frac{r_A}{r_B} = 1.225$ [1,18–22]. But these can also be formed at lower or higher ratios, whereas the hexagonal *C*14 and *C*36 Laves phases occur within smaller ranges between 1.12 to 1.26 while the *C*15 Laves phase ranging between 1.1 to 1.35 [20]. Within their homogeneity range, Laves phases can be formed with deviations from the ideal stoichiometry, exhibiting point defects like antisite atoms or vacancies, which can lead to local lattice strains that may influence mechanical properties [23]. For example, Paufler et al. [24] conducted pioneering macroscopic deformation studies of the *C*14 $MgZn_2$ phase above the BDTT, which revealed a significant effect of composition on mechanical properties, highlighting the importance of understanding the underlying, defect-related mechanisms. A comprehensive review of the influence of internal compositional adjustments and the role of ternary additions in modifying mechanical properties can be found in [25], which we summarise here:

The effects of compositional variations become particularly pronounced in those Laves phases that exhibit large homogeneity ranges, as they can stabilise in multiple defect state modifications. Pseudo-binary Laves phases $(A(B,C)_2$ or $(A,C)B_2)$ — where one sublattice is partially substituted by a chemically similar element — often exhibit extensive homogeneity ranges and are therefore ideal candidates for systematic investigation. Despite their technological relevance, the impact of these often only subtle compositional deviations on phase stability and mechanical behaviour remains only partially understood. Previous investigations demonstrated that small shifts within the homogeneity range can alter defect structures and stacking sequences, thereby modifying hardness, fracture toughness, and even the BDTT. For instance, Takata et al. [26,27] reported a softening effect in *C*14 $NbFe_2$ when the concentration of the smaller B atom was increased, correlating this with planar stacking faults and enhanced dislocation mobility. Similar trends have been reported for the same system, where the Fe-lattice is substituted with Ni, which above ~33 at.% significantly changes the deformation behaviour. These changes were attributed to alteration in the stacking sequences of the triple layers by more abundant formation of stacking faults [28–30]. The Mg–Al–Ca system is well suited for investigating deviations from stoichiometric composition, as calculated homogeneity ranges are available for both the *C*14 and *C*15 Laves phases upon the addition of a third alloying element (Al for *C*14 and Mg for *C*15) [6]. While the influence of ternary alloying on the cubic *C*15 Laves phase has been investigated previously [25], the present study focuses on the corresponding behaviour of the hexagonal *C*14 Laves phase. The *C*14 and *C*15 Laves phases are closely related and share identical structural building blocks, including Kagomé atomic networks and triple layer motifs. The primary distinction between the two structures lies in the stacking sequence of these layers. The triple layers occur along the {111} planes in the cubic *C*15 phase and along the {0001} plane in the hexagonal *C*14 phase. This difference in stacking results in different crystal symmetries while preserving identical local coordination environments. The resulting change in symmetry affects the equivalence and numbers of available slip systems and thereby influences the plastic deformation behaviour. In particular, the lower symmetry of the hexagonal *C*14 phase leads to a more restricted set of equivalent slip planes and a stronger orientation dependence on non-basal slip activation compared to the cubic C15 phase. In addition, differences in stacking and symmetry influence dominant point-defect configurations and the homogeneity range, rendering the mechanical response of the *C*14 phase more sensitive to compositional variations. Investigating how the addition of a ternary element modifies the mechanical properties and plastic response of the hexagonal *C*14 Laves phase therefore meaningfully expands the insights from existing studies on the cubic *C*15 phase and helps to assess the transferability of deformation mechanisms between closely related Laves-phase structures.

Recently, atomic-scale modelling approaches, including density functional theory [31–33] and classical atomistic simulations [25,34,35], have emerged as effective tools for elucidating the influence of chemical variations on structural stabilities and mechanical properties. These methods allow for investigations using perfectly homogeneous and systematically varied compositions with accurate descriptions of interatomic interactions. In particular, atomistic simulations allow the modelling of large atomic configurations for exploring dislocation dynamics under solute-decorated conditions [35], as well as configurations that capture representative chemical randomness for studying solid-solution effects [25]. In this context, atomistic simulations can be employed to explore large parameter spaces and identify compositional regimes in which pronounced changes in behaviour are predicted, which can then be further validated experimentally to confirm the atomistic insights.

In the present work, atomistic simulations using a ternary machine learning moment tensor potential (MTP), were conducted to predict the composition-dependent elastic properties and the energy barriers associated with different slip systems, offering insight into the underlying deformation mechanisms. To validate these predictions, the existing data on near stoichiometric *C*14 $CaMg_2$ [36] was expanded in the direction of the most prominent property change suggested by the simulations. A ternary *C*14 $Ca(Al,Mg)_2$ Laves phase was synthesised and examined using a combination of compositional and microstructural characterisation with nanomechanical testing including a statistical slip-trace analysis and transmission electron microscopy (TEM) to reveal the deformation structures beneath the surface. By directly linking simulation outcomes with experimental observations, this study aims to establish a consistent framework for assessing deformation in Laves phases and to elucidate the effects of composition-induced deviations from the ideal binary state into off-stoichiometric and ternary regimes.

2. Experimental methods

2.1. Atomistic simulations

The atomistic simulations in this study were performed using the open-source Large-scale Atomic/Molecular Massively Parallel Simulator (LAMMPS) [37], with a Mg-Al-Ca MTP interatomic potential [38,39] employed. To evaluate the elastic properties as a function of composition, stiffness tensors were calculated on *C*14 $CaMg_2$ in a wide range of compositional space: Mg replaced by Al up to 2 at. %, Mg replaced by Ca up to 4 at. %, and Ca replaced by Mg up to 4 at. %. Generalised stacking fault energy (GSFE) profiles were calculated for five distinctive *C*14 compositions: the ideal stoichiometric composition ($CaMg_2$), two binary off-stoichiometric ($Ca_{31}Mg_{69}$, $Ca_{37}Mg_{61}$), and two ternary off-stoichiometric compositions, derived from the binary compositions by alloying 2 at.% of Al instead of Mg ($Ca_{33}Mg_{65}Al_2$, $Ca_{37}Mg_{61}Al_2$). The atomic structures of the *C*14 Laves phases were generated using Atomsk [40]. Off-stoichiometric structures were derived from the ideal structure by randomly introducing antisite-type point defects. The supercell sizes and dimensions used in the GSFE calculations are given in Table 1. To address the variability in the mechanical response due to the different configurations of alloying element configurations within the limited size of the simulation cell, five samples with identical overall compositions but distinct elemental distributions were generated. The energy values were then averaged to obtain representative results.

The atomic structures were subsequently relaxed to their minimum energy states using an iterative approach combining conjugate gradient (CG) minimisation for box relaxation and the fast inertial relaxation engine (FIRE) method [41] for ionic relaxation. To determine the zero-temperature elastic stiffness tensor, a series of small elastic strains were systematically applied to the simulation cells, and the resulting stress tensors were computed for each deformation state. GSFE profile calculations were performed with a non-periodic boundary condition in the direction normal to the fault plane (z-axis), while periodic boundary

Table 1
Approximated supercell sizes used in atomistic simulations for GSFE calculations. Cell sizes exhibit slight variations from given values depending on the random seed for alloy generation.

Sample	Slip system	Number of atoms	Cell dimensions [Å^3]
$Ca_{31}Mg_{69}$ $Ca_{37}Mg_{63}$ $Ca_{33}Mg_{65}Al_2$ $Ca_{37}Mg_{61}Al_2$	Prismatic I	3600	20.2 × 18.6 × 269.7
	Prismatic II	2400	20.2 × 21.5 × 155.7
	Pyramidal I	13344	24.8 × 22.8 × 661.5
	Pyramidal II	6240	23.7 × 21.5 × 344.7
$CaMg_2$	Prismatic I	600	10.1 × 6.2 × 269.7
	Prismatic II	600	10.1 × 10.8 × 155.7
	Pyramidal I	3336	6.2 × 22.9 × 661.5
	Pyramidal II	1560	11.9 × 10.8 × 344.7

conditions were maintained in the in-plane directions. Fig. 1 shows the slip systems and corresponding interlayers selected for the GSFE sampling. In each simulation, atoms in the upper half of the simulation cell were incrementally displaced by a defined offset in the slip directions. After each displacement step, the faulted structure was minimised along the z-direction using the FIRE method. The GSFE value was calculated according to Eq. (1):

$$\gamma_{GSF} = \frac{(E_f - E_i)}{l_x \cdot l_y}, \quad (1)$$

where E_i and E_f denote the potential energies of the pristine and faulted structures, respectively, and l_x and l_y denote the dimensions of the simulation cell in the x and y directions. Atomic visualisations were conducted using OVITO [42].

The interlayer with the lowest unstable stacking fault energy (γ_{USF}) was determined for each slip system using the stoichiometric composition. GSFE scanning was then performed on the same minimum-energy interlayers for the off-stoichiometric compositions. The corresponding layers were III, II, I and I for the prismatic I $\langle c \rangle$, prismatic I $\langle a \rangle$, prismatic II $\langle \bar{1}100 \rangle$ and prismatic II $\langle c \rangle$ slip, respectively, and layers I, III, I, and I for the pyramidal I $\langle a + c \rangle$, pyramidal I $\langle a \rangle$, pyramidal II $\langle a + c \rangle$, and pyramidal II $\langle \bar{1}100 \rangle$ slip systems, respectively.

2.2. Microstructural characterisation

In order to investigate the influence of off-stoichiometry on the mechanical behaviour of *C*14 Laves phases in the Mg–Al–Ca system, a bulk polycrystalline sample was synthesised with a composition close to that predicted by atomistic simulations. Owing to the limited homogeneity ranges of the relevant intermetallic phases and the uncertainties in ternary phase equilibria over the temperature range from the melt to solidification, a bulk synthesis route combined with slow solidification was deliberately chosen to promote chemical equilibration and the formation of coarse microstructures. An ingot with $Ca_{32.7}Al_{31.9}Mg_{35.4}$ was given in a tantalum ampoule and synthesised using the Bridgman method in accordance with the procedure described [25,43]. During this synthesis the melt was separated and crystallised as two different samples, one sitting in the bottom of the ampule and the other on the top. The sample on the top reveals as main phase the off-stoichiometric *C*15 Laves phase with a composition of $Ca_{38}Al_{51}Mg_{11}$ and the bottom part the in this study analysed $Ca_{37}Mg_{61}Al_2$ *C*14 Laves phase.

Initially, the as-cast specimen was embedded in a copper-based paste and prepared systematically for further analysis. This entailed five sequential grinding steps, culminating in a final abrasive of grit size of 4000, followed by mechanical polishing. Polishing was conducted using diamond pastes of decreasing grain sizes, ranging from 6 μm to 0.25 μm on a STURERS MD DAC cloth. A lubricant containing 5 % polyethylene glycol (PEG) in ethanol was used. Final polishing was performed in two stages: the first stage used a 7 % OP-A suspension (consisting of 7 % dispersed alumina in isopropanol with 5 % PEG), and the second stage

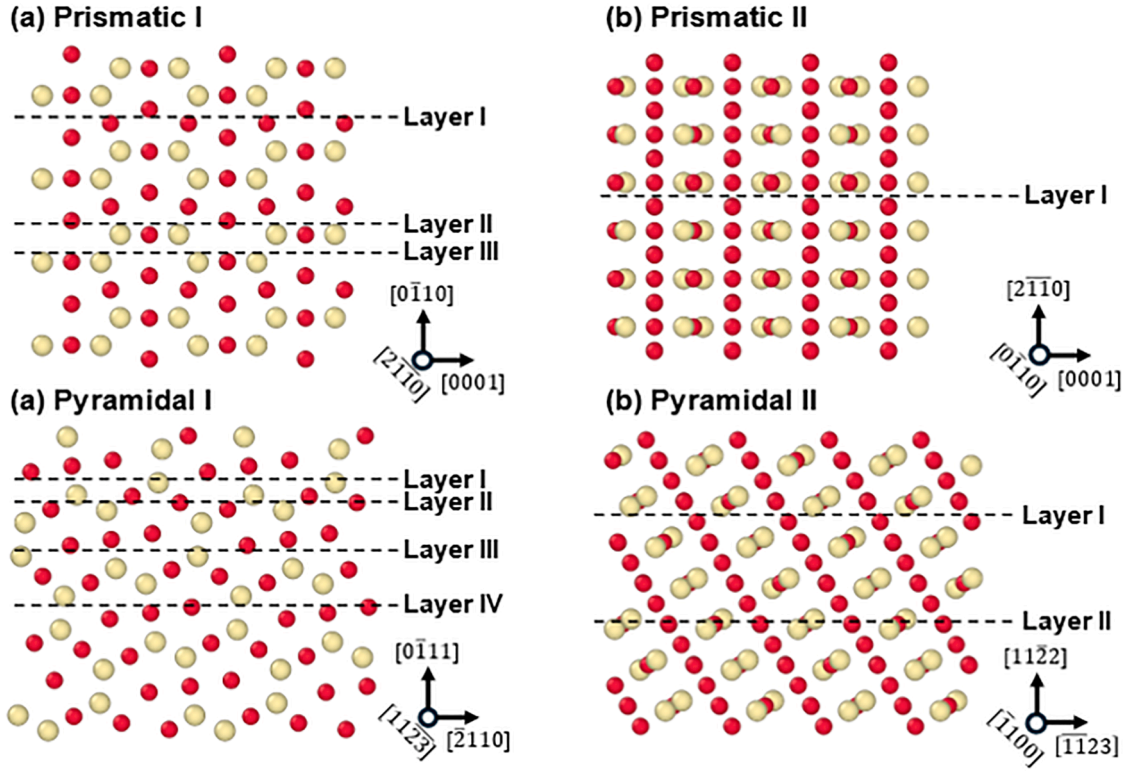


Fig. 1. Slip systems and corresponding interlayers selected for GSFE sampling. Yellow (larger) and red spheres (smaller) represent Ca and Mg atoms, respectively.

involved cleaning with water and a detergent solution. Phase compositions were determined using energy dispersive x-ray spectroscopy (EDS) (Helios Nanolab 600i, FEI). The measured compositions for all the investigated regions were 60.46 ± 0.08 at.% Mg, 37.39 ± 0.10 at.% Ca, and 2.15 ± 0.04 at.% Al. The resulting material exhibits a polycrystalline microstructure with large grains, enabling a systematic investigation of orientation-dependent mechanical and micromechanical properties by nanoindentation.

2.3. Nanoindentation experiments

Nanoindentation experiments were conducted to quantify both the elastic properties and the plastic deformation behaviour. The tests were performed using a load-controlled iNano nanoindenter (Nanomechanics Inc., TN, USA), which was equipped with a diamond Berkovich tip (Synton MDP, Switzerland), and a dynamic indentation unit employing continuous stiffness measurement (CSM). Instrument calibration was achieved by referencing a fused silica standard and employing the Oliver and Pharr method to determine the diamond area function (DAF) and frame stiffness [44,45]. A total of 175 indents were performed under identical conditions, with a constant strain rate of 0.2 s^{-1} up to a maximum depth of 500 nm. Data analysis extraction of the indentation modulus and hardness, taken over a measured range between 350 – 500 nm depth, as well as identification of activated slip systems. Correlation between the slip traces (from scanning electron microscopy (SEM) images (CLARA, Tescan, Brno, Czech Republic)) and the grain orientation information (from electron backscattered diffraction (EBSD) (Hikari, EDAX Inc., CA, USA)) was performed in accordance with the methodology described by Gibson et al. [46].

2.4. TEM experiments

A TEM lamella was prepared across an indented region, using site-specific focussed ion beam (FIB) milling (Helios Nanolab 600i, FEI). This lamella was then examined using TEM (JEOL JEM-F200 and FEI – Tecnai G^2 F20 S-TWIN) in various two-beam conditions.

3. Results

3.1. Atomistic simulations

Based on the stiffness tensors calculated using the interatomic potential, the elastic properties, including Poisson's ratio (ν), elastic modulus (E), shear modulus (G), and bulk modulus (K), of $C14$ Ca-Mg-Al Laves phases across a wide compositional range were evaluated – reflecting simultaneously the dependence on A:B (Ca:Mg) ratio in terms of deviations from the ideal AB_2 stoichiometry as well as the additional effect of substitution on the B sites (Al for Mg).

The variations in the investigated elastic properties relative to the stoichiometric $C14$ $CaMg_2$ are shown in Fig. 2. Three substitutional configurations were considered: Mg replaced by Al up to 2 at.% (Al_{Mg} on the y-axis), Mg replaced by Ca up to 4 at.% (Ca_{Mg}, left side of the x-axis), and Ca replaced by Mg up to 4 at.% (Mg_{Ca}, right side of the x-axis). Deviations from stoichiometry induced by Ca_{Mg} and Mg_{Ca} substitutions lead to an overall decrease in the elastic moduli. Moreover, an asymmetric response is observed: Ca_{Mg} antisite defects lead to a more pronounced compliance than Mg_{Ca} substitutions at the same concentrations. In contrast, Al substitution for Mg (Al_{Mg}) induces a stiffer response. However, as evident from Fig. 2(b)-d)), the stiffening effect of Al on the B site is relatively minor compared to the dominant compliance effect caused by Ca_{Mg} or Mg_{Ca} substitutions. The effect on Poisson's ratio is also less significant, with Ca_{Mg} and Mg_{Ca} substitutions causing only a slight increase from 0.24 to 0.25.

The stiffness tensors and elastic moduli of selected binary and ternary $C14$ Ca-Mg-Al Laves phases are summarized in Table 2. The binary compositions show a decreasing trend in elastic moduli with increasing deviation from the stoichiometric AB_2 composition, on both the Ca- and Mg-rich sides. The change caused by decreasing the Ca atomic fraction (or increasing the Mg atomic fraction) has a relatively small influence on the elastic properties, as illustrated by $Ca_{31}Mg_{69}$ (composition 1), where all changes remain below 1 GPa and of the order of 2.2 % at most. In contrast, $Ca_{37}Mg_{63}$ (composition 3), with an increased Ca atomic fraction (or decreased Mg atomic fraction), shows a pronounced reduction in elastic properties, approximately 5 %, 9 %, and 9 %, for K, E, and G, respectively, compared to the stoichiometric

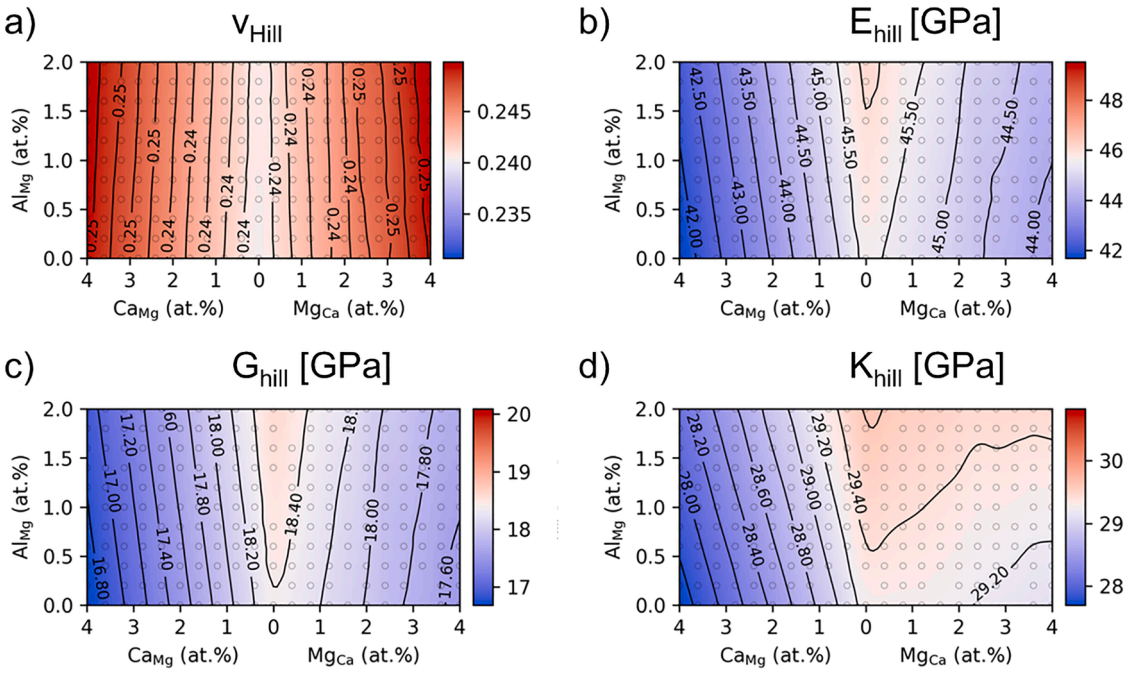


Fig. 2. Variations in the elastic properties with composition for the $C14$ Laves phases: a) the Poisson's ratio ν_{Hill}, b) the elastic modulus E_{Hill}, c) the shear modulus G_{Hill}, and d) the bulk modulus K_{Hill}. Al_{Mg} denotes substitution of Mg by Al, Ca_{Mg} substitution of Mg with Ca, and Mg_{Ca} substitution of Ca by Mg.

Table 2
Stiffness tensor components and elastic moduli of the simulated stoichiometric and off-stoichiometric *C*14 Laves phases.

Composition	C_{11} (GPa)	C_{12} (GPa)	C_{13} (GPs)	C_{33} (GPa)	C_{44} (GPa)	C_{66} (GPa)	K_{Hill} (GPa)	E_{Hill} (GPa)	G_{Hill} (GPa)	ν_{Hill}
Binary *C*14 Laves phases										
1. $Ca_{31}Mg_{69}$	54.35	17.48	15.93	55.61	16.67	18.44	29.23	44.77	17.98	0.24
2. $CaMg_2$	54.84	17.29	15.81	55.86	17.22	18.77	29.26	45.60	18.39	0.24
3. $Ca_{37}Mg_{63}$	51.04	16.69	15.45	51.93	15.46	17.21	27.69	41.68	16.68	0.25
Ternary *C*14 Laves phases										
4. $Ca_{33}Mg_{65}Al_2$	55.44	17.50	16.03	56.49	17.41	18.98	29.62	46.10	18.58	0.24
5. $Ca_{37}Mg_{61}Al_2$	51.94	16.98	15.80	52.68	15.73	17.44	28.19	42.35	16.94	0.25

composition.

The influence of an additional alloying element, Al, was examined through calculations on the ternary *C*14 Laves phases. In $Ca_{33}Mg_{65}Al_2$ (composition 4), 2 at.% of Mg atoms is substituted by Al. In $Ca_{37}Mg_{61}Al_2$ (composition 5), Mg is substituted both by 4 at.% Ca (Ca_{Mg}) and by 2 at. % Al (Al_{Mg}). Composition 4, containing only Al_{Mg} substitution, shows a negligible increase in the elastic moduli. In contrast, composition 5, with an additional Ca_{Mg} substitution, exhibits a clear decreasing trend compared to the stoichiometric composition (composition 2). This is therefore the composition we selected for further investigations by experiments in addition to the already available experimental data on near stoichiometric $CaMg_2$.

The elastic anisotropy of the hexagonal *C*14 Laves phase was evaluated to assess its potential influence on the measured indentation modulus. The universal elastic anisotropy index (A_U) of the investigated compositions is approximately 0.017, indicating that the material is close to elastically isotropic. As expected, the indentation modulus as a function of crystallographic orientation (calculated using the Vlassak–Nix model) [47], reveals only minor variations and no significant change in the anisotropy profile across the compositional range studied (see Figure S1).

The GSFE profiles and corresponding unstable stacking fault energies γ_{USF} for various slip systems in stoichiometric and off-stoichiometric *C*14 Ca-Mg-Al Laves phases are shown in Figure S2 and Table S1 of the Supplementary Material. The γ_{USF} value was calculated for the $\langle a \rangle$ slip directions on the prismatic and pyramidal 1st order planes (marked by circles in Fig. 3), for the $\langle c \rangle$ slip directions on the prismatic planes (diamond symbol in Fig. 3), for the $\langle \bar{1}100 \rangle$ slip directions on the prismatic and pyramidal 2nd order planes (inverted triangle in Fig. 3), and for the $\langle c+a \rangle$ slip directions on the pyramidal planes (squares in Fig. 3). Note that this set of simulations does not include the basal plane. The reasons for this are as follows: (i) with synchroshear the expected dislocation mechanism in the triple layer along the basal plane, simple shearing, as performed in calculations of the GSFE and the corresponding unstable stacking fault energies from this data, is not adequate for synchroshear, due to its multidirectional and multiplanar nature [48, 49], (ii) calculations of the barrier to dislocation motion and unstable configurations are possible but require significantly larger cells and consideration of the dissociation of the synchroshear partials [35,41, 50]; achieving direct comparability between the datasets on the different slip systems would therefore significantly increase computational effort for all slip systems; (iii) in experiments on the binary composition using micropillar compression, the critical resolved shear stress (CRSS) on the basal slip was found to be of intermediate magnitude, and a corresponding slip trace analysis confirmed this ranking of active slip systems [36], so that (iv) basal slip, with its single available slip plane (as opposed to the multiple prismatic and pyramidal planes) is expected to have a limited contribution to multiaxial deformation.

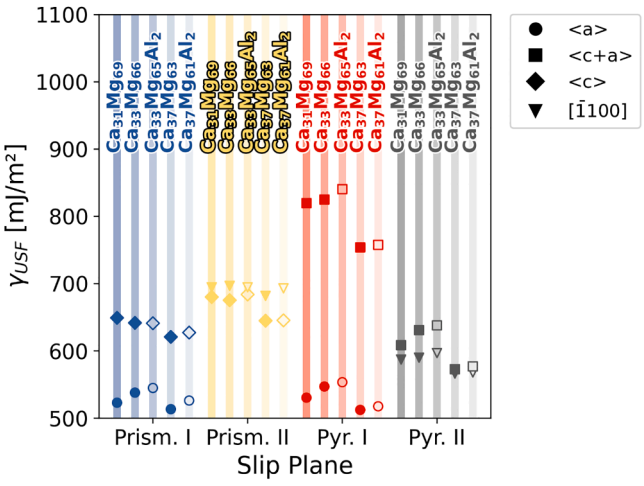


Fig. 3. Unstable stacking fault energies γ_{USF} for selected slip systems in *C*14 Ca–Mg–Al Laves phases. The γ_{USF} values (in mJ/m²) are shown for prismatic 1st (blue), prismatic 2nd (yellow), pyramidal 1st (red), and pyramidal 2nd (grey) ordered planes in $Ca_{31}Mg_{69}$, $Ca_{37}Mg_{63}$, $Ca_{37}Mg_{63}$, $Ca_{33}Mg_{65}Al_2$, and $Ca_{37}Mg_{61}Al_2$. The filled symbols presenting the values with only binary changes and the unfilled the ternary. Symbols denote slip directions: circles – $\langle \boldsymbol{a} \rangle$, squares – $\langle \boldsymbol{c}+\boldsymbol{a} \rangle$, diamonds – $\langle \boldsymbol{c} \rangle$, and inverted triangles – $[\bar{1}100]$.

The lowest γ_{USF} values among all non-basal slip systems are found for the 1st-order slip planes with $\langle a \rangle$ slip directions, ranging between 510 and 550 $\frac{mJ}{m^2}$ Interestingly, the γ_{USF} value for the secondary $\langle c+a \rangle$ slip direction on the 1st order pyramidal plane deviates by approximately 300 $\frac{mJ}{m^2}$, from the $\langle a \rangle$ slip direction, representing the highest values among all slip systems. For the prismatic 1st order slip systems, the secondary $\langle c \rangle$ slip direction exhibits γ_{USF} deviation about 100 $\frac{mJ}{m^2}$ higher than that of the $\langle a \rangle$ slip direction. In contrast, the differences among the possible slip directions of the 2nd order planes are relatively small: the pyramidal 2nd order slip systems reveal γ_{USF} values between 560 and 640 $\frac{mJ}{m^2}$, while the prismatic 2nd order systems range from 640 to 700 $\frac{mJ}{m^2}$

When comparing the different compositions, it is evident that those with higher Ca content, specifically $Ca_{37}Mg_{63}$, followed by $Ca_{37}Mg_{61}Al_2$, exhibit the lowest γ_{USF} values across most slip systems. In general, a reduction in γ_{USF} is observed with deviation from the ideal AB_2 composition, that is both for Ca_{Mg} or Mg_{Ca} substitutions, apart from the case of $\langle c \rangle$ slip, where softening with increasing Ca content across all three compositions. The addition of Al increases γ_{USF} for all slip systems, except the prismatic 1st $\langle c \rangle$ and prismatic 2nd order slip systems, where the effect of Al addition is negligible. These softening and hardening effects induced by substitution between Ca and Mg and addition of Al, respectively, also agree well with the trends observed in the elasticity space. The consistently low γ_{USF} values observed for the pyramidal and prismatic 1st order $\langle a \rangle$ slip systems indicate that these are the most energetically favourable among the investigated non-basal deformation modes across all compositions. Furthermore, our observation suggests that compositional variations primarily modulate, rather than alter, the preferred slip activity, and that off-stoichiometry may enhance resistance to dislocation motion along specific directions, thereby influencing the alloy's overall plastic anisotropy.

3.2. Nanoindentation

Nanoindentation experiments performed on the $Ca_{37}Mg_{61}Al_2$ regions yielded an average hardness of 2.3 ± 0.1 GPa and an average indentation modulus of 43.9 ± 1.3 GPa. These values were extracted from measurements taken between penetration depths of 350 nm and 500 nm, assuming a Poisson's ratio of 0.24. Especially for hexagonal systems, the anisotropy regarding the hardness or indentation modulus should be analysed. In this context inclination angle, the misorientation between the loading direction and the c-axis, is included as the elastic anisotropy governed by inclination angle in hexagonal crystals rather than axial rotation along c-axis. No dependency was observed either for the hardness or the modulus. Detailed results are shown in Table 3, where the different areas from A to F correspond to the different orientations of the nanomechanical measurements and indentation slip line analysis, shown in Fig. 4 and the analysis results in Fig. 5.

3.3. Surface trace analysis

Representative SEM images of nanoindentation-induced deformation are presented in Fig. 5. All indents exhibit evidence of crystallographic slip. A total of 1974 slip traces were analysed to evaluate their alignment with the crystallographic slip planes within the unit cell. Crystallographic orientation data obtained by EBSD were correlated with the orientation of surface slip traces observed around the indentation sites. For a clear assignment of surface features to specific slip planes, only traces exhibiting a well-defined linear character were considered. Accordingly, the analysis was restricted to surface features that could be classified as either straight lines or edges [51–53]. Here, straight lines denote slip traces that remain linear over their entire observable length, whereas edges refer to traces that exhibit a distinct change in direction but subsequently continue as a straight segment. Slip traces exhibiting curvature, as indicated in Figure A and Figure C, were excluded from the dataset. The absence of cracks in the examined areas confirms that the identified surface traces are solely attributable to plastic deformation. Figure illustrates representative examples of the surface traces corresponding to all six crystallographic orientations. Figure S2 presents the associated slip system activation frequencies.

In order to elucidate the effect of compositional modifications on plasticity, the present results for the ternary *C*14 Laves phase (Fig. 4a) were compared with the previously reported data for the binary *C*14 Laves phase from Zehnder et al. [36], presented in Fig. 4b). In Fig. 4a)-b), the overall occurrence of slip traces assigned to a given type of slip plane is shown as a function of the inclination angle between compression axis and c-axis for the Ca-rich ternary *C*14 phase investigated here (Fig. 4a) as well as the binary Ca-poor *C*14 phase $Ca_{31}Mg_{69}$ (Fig. 4b) investigated previously [36].We note that the total number of analysed surface traces differs by a factor of ~9 (217 traces analysed in [36]). For $Ca_{37}Mg_{61}Al_2$, the pyramidal systems dominate, while the basal slip system remains the lowest in terms of observed slip traces over the entire inclination range despite a maximum at 53°, confirming its limited contribution to multiaxial deformation. Compared with the of $Ca_{31}Mg_{69}$ composition, the addition of 2 at.% Al and an increase of Ca content result in a more homogeneous distribution of the pyramidal and prismatic systems with little dependence on inclination, and a reduced preference for a specific pyramidal system. In contrast, a more pronounced dependence on inclination angle is found in $Ca_{31}Mg_{69}$ particularly for the first order prismatic plane.

Looking at the overall activation frequencies (Fig. 4c), both alloys show minor basal activity. In contrast to the ternary alloy, the $Ca_{31}Mg_{69}$ alloy exhibits round about twice the activation frequency regarding the prismatic 1st order planes, consistent with the findings of the micropillar compression tests, showing this as the system with the lowest critical resolved shear stress (CRSS) which is therefore easiest activatable system [36].

Table 3
Chemistry, hardness and indentation modulus of all orientations, with the standard deviations rounded to the first decimal place, labelled from A to F with corresponding inclination angle.

Area	Inclination angle	Chemical composition			Hardness [GPa]	Indentation Modulus [GPa]
		Mg [at. %]	Al [at. %]	Ca [at. %]		
A	19°	60.4 ± 0.1	2.1 ± 0.1	37.4 ± 0.1	2.5 ± 0.1	43.2 ± 1.5
B	34°	60.5 ± 0.1	2.2 ± 0.1	37.3 ± 0.2	2.4 ± 0.0	46.1 ± 0.7
C	45°	60.3 ± 0.1	2.1 ± 0.1	37.6 ± 0.1	2.4 ± 0.1	44.2 ± 1.6
D	53°	60.4 ± 0.3	2.1 ± 0.1	37.5 ± 0.1	2.4 ± 0.0	46.0 ± 0.4
E	60°	60.5 ± 0.3	2.2 ± 0.1	37.3 ± 0.3	2.3 ± 0.1	43.9 ± 1.3
F	78°	60.6 ± 0.3	2.2 ± 0.1	37.3 ± 0.3	2.2 ± 0.6	44.0 ± 1.7

3.4. TEM experiments

A TEM lamella was prepared from the deformation zone beneath a residual indent from area A to analyse the post-deformation microstructure. Four zone axes were reachable for this TEM analysis, namely the $[0\bar{1}11]$, $[0\bar{3}31]$, $[0\bar{1}10]$ and $[\bar{1}\bar{1}20]$. The lamella itself was slightly bent (around 3°), from its centre to the edges, presumably due to the residual stresses from indentation (Fig. 6).

Fig. 5 shows the overview of the dislocation structure in the lamella imaged along the $[\bar{1}\bar{1}20]$ zone axis, revealing edge-on dislocations towards the upper right corner, which are found to lie parallel to the pyramidal 1st order $(1\bar{1}01)$ (in dark green) and prismatic 1st order $(1\bar{1}00)$ (red) planes. Additionally, the prismatic 1st order $(1\bar{1}00)$ slip traces run along >10 parallel traces. Interestingly, some of them fade with increasing distance from the high pressure centre of the indentation, whereas one changes plane onto the pyramidal 1st order $(1\bar{1}01)$ plane (marked in light green), and another aligns with a feature lying parallel to the $(1\bar{1}02)$ plane (marked in blue) at a position slightly below the first but closer to the centre of the indentation. All four planes are visualised within the unit cell aligned along the same zone axis as the images, Fig. 5c).

4. Discussion

In this section, the results obtained for five simulated Laves-phase compositions are dis-cussed and directly compared with available experimental data for $Ca_{31}Mg_{69}$, available from ref [36], and $Ca_{37}Mg_{61}Al_2$, as a composition that was both experimentally accessible and expands experimental data into the ternary regime.

4.1. Compositional characterisation and phase identification

The primary objective of this study is to evaluate the influence of compositional modifications on the mechanical properties of the hexagonal $CaMg_2$ Laves phase. In particular, we aimed to investigate experimentally those compositions predicted to exhibit maximum ductility and/or mechanism changes compared with the binary, Ca-poor $Ca_{31}Mg_{69}$ composition already reported in the literature [36]. EDS measurements performed on both, bulk sample and TEM lamellae, confirmed the intended compositional deviation from the stoichiometric

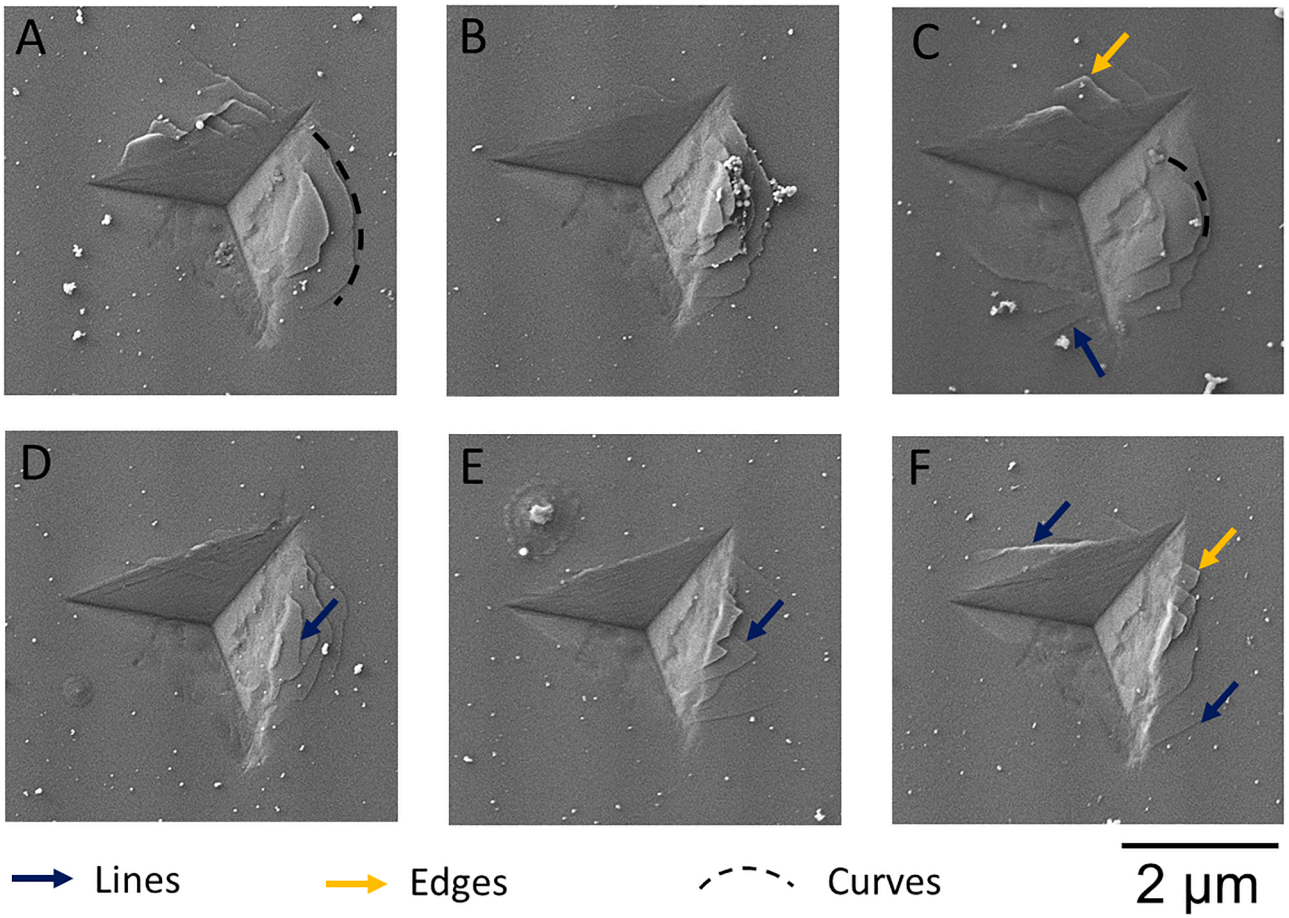


Fig. 4. Surface slip traces observed in six differently oriented indentation areas. Area C (inclination angle of 45°) shows all features: straight lines (indicated by blue arrows), edges (yellow arrows) and curves (curved black dashed line). Area B and Area D with inclination angles slightly above and below 45° reveal predominantly curved traces, but also straight lines could be found. Area E and Area F (60 and 78°) show a combination of straight lines and curves, whereas Area A (19°) has both curves and edges.

composition, characterised by a reduction in Mg content of approximately 6 at.% and a concomitant increase in Ca content of around 4 at. %, as well as the presence of 2 at.% Al.

Previous investigations into the homogeneity range of ternary Laves phases have primarily focused on varying only two of the three constituent elements. Thus, compositions involving the simultaneous adjustment of all three elements have not been explored or reported in detail until now. Earlier work by Amerioun et al. [6] examined phase stability by altering Mg and Al contents while keeping the Ca content constant. They found that the *C*14 phase is stable for Mg contents between 55.5 at.% and 66.6 at.%, and Al contents ranging from 16.2 at.% to 0 at.%. Complementary studies by Tehranchi et al. [32], who used density functional theory, suggested a slightly wider compositional range extending to 43.3 at.% Mg and 23.3 at.% Al.

The identification of the *C*14 Laves phase in the present study was confirmed by correlating EBSD Kikuchi patterns with those expected for the stoichiometric phase (yielding a confidence index of 0.85). Alternative fits to the *C*36 $Ca(Mg,Al)_2$ and the *C*15 $CaAl_2$ Laves phase yielded lower confidence values. The presence of the *C*14 structure was further corroborated by selected area electron diffraction (SAED) patterns obtained from TEM lamellae (Fig. 5), unambiguously exhibiting reflections corresponding to the hexagonal Laves phase.

4.2. Mechanical softening by compositional modification

Atomistic simulations reveal that off-stoichiometric modifications in the *C*14 $CaMg_2$ Laves phase substantially influence both its elastic and plastic responses, namely increasing the Ca atomic fraction results in reduced elastic stiffness and lower γ_{USF}. The ternary $Ca_{37}Mg_{61}Al_2$ composition is calculated to have an approximately 4 % reduction in Young's modulus and an 8 % reduction in shear modulus relative to stoichiometric $CaMg_2$. This compliance effect is primarily associated with atomic substitutions, particularly Ca atoms occupying the Mg sublattice, as the formation of Ca_{Mg} anti-site defects is more energetically favourable than Mg vacancies in accommodating Ca-rich off-stoichiometry [55]. Moreover, Ca_{Mg} substitutions reduce the γ_{USF} values of non-basal slip systems in Ca-enriched compositions (see Fig. 3). In contrast, substitution between Mg and Al, elements with similar atomic radii, produces only minor stiffening and strengthening effects ($\leq$ 3 %). The decreased γ_{USF} implies lower critical stresses for dislocation activation, facilitating the motion of non-basal dislocations and enhancing plastic accommodation. Consequently, Ca enrichment correlates with reduced stiffness and lower barriers to dislocation motion, providing an atomistic basis for the experimentally observed softening.

Nanoindentation measurements yield an average hardness of 2.4 $\pm$ 0.3 GPa and an indentation modulus of 50.0 $\pm$ 1.9 GPa for $Ca_{37}Mg_{61}Al_2$, representing a ~29 % decrease in hardness and ~9 % reduction in indentation modulus compared to the binary $Ca_{31}Mg_{69}$ phase (3.4 $\pm$ 0.2 GPa and 55.1 $\pm$ 3.0 GPa [36]).

The elastic modulus of the off-stoichiometric *C*14 phase decreases from 55.1 GPa to 50.0 GPa, corresponding to a reduction of approximately 9 %. Although this experimentally observed compliance exceeds the atomistically predicted value of ~4 %, the difference is only marginally resolved within the experimental scatter, with a combined

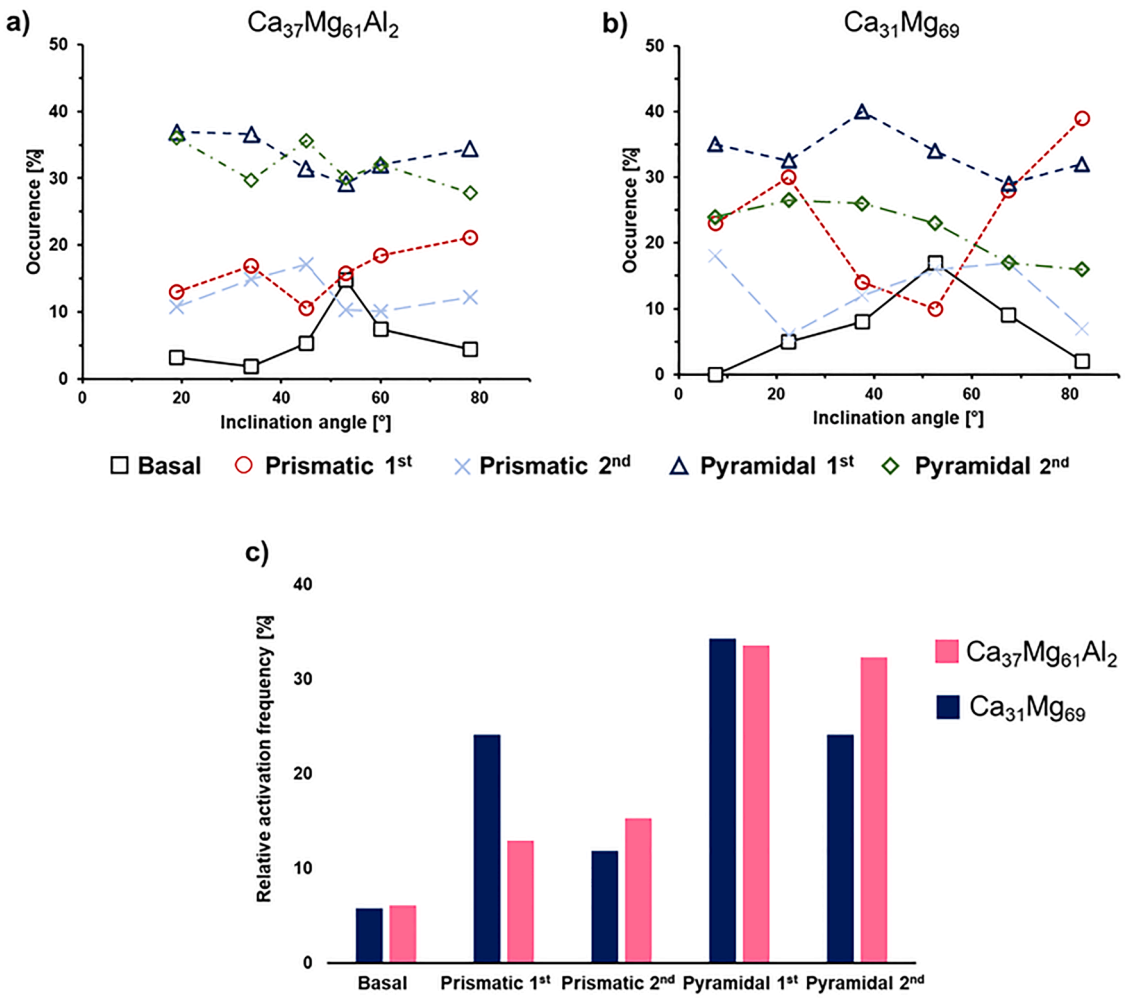


Fig. 5. Inclination angle dependence and relative slip activation frequencies for Ca–Mg–Al alloys. a) and b) show the occurrence of different slip systems— basal (black □), prismatic 1st (light blue X), prismatic 2nd (red°), pyramidal 1st (dark blue △) and pyramidal 2nd (green ⋄) as a function of inclination angle for a) $Ca_{37}Mg_{61}Al_2$ and b) $Ca_{31}Mg_{69}$. c) presenting the activation frequency over all analysed orientations.

uncertainty of 3.6 GPa. The calculated modulus reduction is therefore of comparable order and lies within the range defined by the experimental uncertainty on the modulus difference. In addition, the atomistic simulations assume a random distribution of antisite point defects and Al solutes occupying energetically favourable B sites and do not account for possible chemical short-range ordering or solute clustering that may exist in the experimental materials and influence the effective elastic response. Consequently, the difference in magnitude between the reductions in modulus in experiment and simulation is consistent within the uncertainties of both methods. The hardness decreases by approximately one third, a much larger variation than predicted for the unstable stacking fault energies of less than ~10 %. This difference reflects the fact that nanoindentation hardness is an integral property that reflects the collective response of competing slip systems and several deformation mechanisms under a highly constrained, multiaxial stress state at finite temperatures. As such, even a modest reduction in the barrier for these secondary slip systems can activate additional pathways for plastic flow, thus, accommodating the indentation strain gradient more efficiently. In contrast, the unstable stacking fault energy represents the lattice resistance to crystallographic slip in an ideal crystal at 0 K. Although it is widely used as a descriptor for crystal plasticity, it does not capture dislocation dynamics, in particular dislocation-point defect interactions, where point defects can play a significant role in reducing activation barriers of rate-limiting processes such kink-pair nucleation [34]. While we therefore cannot predict or correlate the magnitude of any change in hardness based on the available data, we note that the change is consistent between experiments and simulations and that, given the significant reduction in hardness in the experiment, future work is warranted to better understand the intricate connections between dislocation plasticity and hardness in the presence of point defects.

These findings are consistent with trends observed in related systems. In our previous study on the cubic *C*15 $CaAl_2$ Laves phase's modulus [25,56,57], substitution of Mg_{Al} induced negligible changes in elastic stiffness, whereas additional Ca_{Al} substitution led to a pronounced drop in hardness and modulus, suppression of crack nucleation, and increased dislocation density with evident cross-slip activity. Atomistic modelling confirmed a more pronounced reduction in energy barriers for most slip systems in Ca-enriched compositions than in compositions enriched with smaller elements (Mg or Al), by deviating from the stoichiometric composition in both hexagonal and cubic Laves structures. Comparable alloying-induced weakening has already been reported in $NbFe_2$-based Laves phases: Takata et al. [27] observed that Ni addition led to an Fe-rich phase ~1 GPa softer than its stoichiometric counterpart. Similarly, Takasugi et al. [28] demonstrated that substituting B-site atoms with those of comparable size to the A-site atoms significantly reduced the brittle-to-ductile transition temperature. This behaviour was attributed to lattice dilation and weaker interatomic bonding, which decrease lattice friction stress and facilitate dislocation nucleation and glide. In the present *C*14 Ca-rich Laves phases, the larger

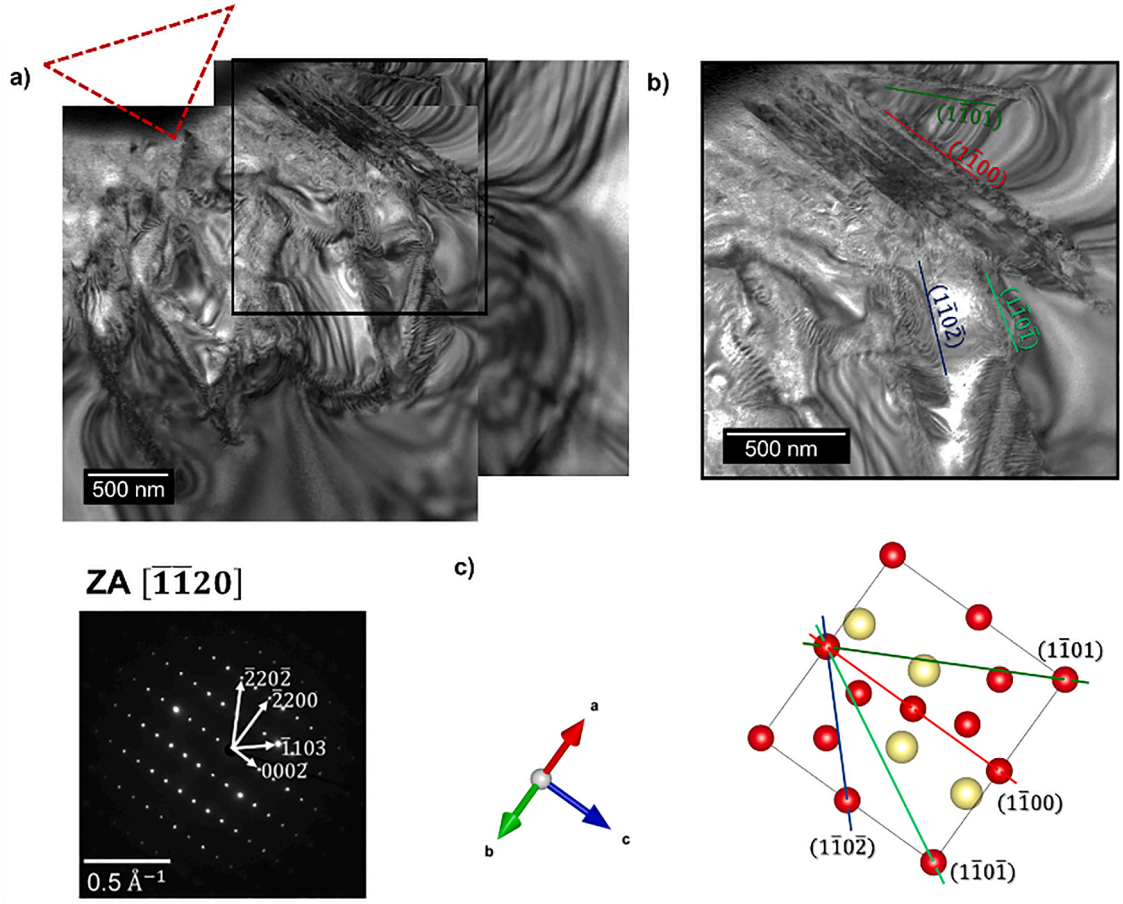


Fig. 6. Dislocation structure beneath the indentation zone in $Mg_{61}Ca_{37}Al_2$ taken from Area A. a) Shows the overview TEM bright field (BF) image taken along the [$\bar{1}\bar{1}$20] zone axis, the red dashed triangle illustrates the placing of the indenter, with b) giving a magnified view of the right edge of the plastic zone. The red line shows slip bands lying edge on to the (1$\bar{1}$00) plane, the dark green lying parallel to the (1$\bar{1}$01) plane, the light green show slip bands lying edge on to the (1$\bar{1}$0$\bar{1}$) plane and the blue line lying parallel to the (1$\bar{1}$0$\bar{2}$) plane. All represented in c) the unit cells with the indexed slip planes using VESTA [54].

atomic radius of Ca compared to Mg and Al likely disrupts the local atomic environment in a similar way, reducing the Peierls barrier and thereby enhancing dislocation mobility.

Together, these findings indicate that introducing larger-radius atoms into the B-sublattice of AB_2-type Laves phases promotes lattice dilation, increases dislocation mobility, and facilitates the activation of non-basal plasticity mechanisms. However, as demonstrated by Zhu et al. [19] the mechanical response of off-stoichiometric Laves phases critically depends on the type, distribution, and site occupancy of point defects and their interaction with dislocation cores. Depending on these parameters, deviations from stoichiometry may result in either softening or hardening, and the controlling factors remain insufficiently understood. The experimentally observed reduction in hardness in the $Ca_{37}Mg_{61}Al_2$ composition compared with binary $Ca_{31}Mg_{69}$ mirrors this behaviour.

4.3. Non-basal slip mechanisms

Considering the simulations on all non-basal slip systems and experiments comparing dislocation activity on all slip planes, we further discuss the effect of composition on slip system activation.

Basal slip consistently exhibited the lowest activation frequency in all compositions during room temperature nanoindentation. In part, this is due to there being only one basal plane, whereas the non-basal planes include up to three crystallographically equivalent, conjugated prismatic and six pyramidal planes. The comparatively small role of basal slip is further thought to arise from the thermally activated nature of the synchroshear mechanism, which is the most energetically favourable deformation mode on this plane [50]. Although the presence of alloying elements can effectively reduce the barrier for basal dislocation motion [35], its activation still requires substantial thermal assistance, making it one of the harder to activate slip systems with an intermediate CRSS [36] and limiting the role of basal slip in plastic deformation at ambient conditions. Consequently, *C*14 Laves phases primarily rely on the activation of non-basal dislocations to accommodate plastic strain and we therefore focus primarily on these systems here, which are also accessible to directly comparable atomistic simulations owing to the absence of the synchroshear mechanism with its partials moving on different parallel planes.

Previously, micropillar compression tests have been used to determine the CRSS of individual non-basal slip systems, indicating that prismatic 1st order slip exhibits the lowest CRSS, followed by pyramidal 1st order slip, while pyramidal 2nd order slip is least active [36]. In contrast, the present nanoindentation based slip trace analysis does not provide direct access to absolute CRSS values but instead reflects the relative activation frequencies of competing slip systems across a broad range of crystallographic orientations. Within this framework, the substitution of Mg by Al and Ca is associated with a redistribution of slip activity, in which prismatic 1st order slip is activated less frequently after basal slip, while the relative activity pyramidal 2nd order slip increases. These observations indicate that alloying influences the relative ease of activation of different slip systems under indentation. However, we cannot draw direct conclusions concerning the absolute CRSS values without uniaxial sampling of each individual slip system.

The activation of pyramidal $\langle c+a \rangle$ slip systems is highly orientation dependent for hexagonal structures. In the hexagonal lattice, basal and prismatic $\langle a \rangle$ dislocations have Burgers vectors confined to the basal plane and thus cannot accommodate strain components along the c-axis. Consequently, deformation along this direction requires the activation of $\langle c \rangle$ or $\langle c+a \rangle$ dislocations on prismatic or pyramidal planes. They play a critical role in enabling three-dimensional plasticity. In the case of $Ca_{37}Mg_{61}Al_2$, the prismatic and pyramidal activity remains comparatively constant across the investigated inclination angles and overall, their ratio of activation frequency corresponds to that of the number of crystallographically equivalent planes, suggesting limited orientation dependence of flow and similar critical stresses. In contrast, the binary $Ca_{31}Mg_{69}$ shows a distinct increase in prismatic 1st order slip planes at high inclination angles. This behaviour suggests a preferential activation of $\langle c \rangle$ slip on prismatic planes, providing more favourable deformation than pyramidal systems, which accommodate c-axis strain via $\langle c+a \rangle$ dislocations. The comparison indicates that Ca and Al additions modify the relative energy barriers between non-basal slip systems, reducing the disparity between pyramidal and prismatic slip in the ternary alloy and thereby promoting more isotropic plastic response compared to the binary $Ca_{31}Mg_{69}$ composition.

These experimental results are consistent with the γ_{USF} energies calculated for the non-basal planes, where pyramidal 1st order and prismatic 1st order $\langle a \rangle$ slip systems have similarly low energy barriers, suggesting a competitive interaction between these slip mechanisms in accommodating $\langle a \rangle$-type strain. This is consistent not only with our slip trace analysis on the Ca-rich and Al-alloyed *C*14 phase but also with our TEM observations presented in Fig. 5, which clearly identify parallel slip bands characteristic of the pyramidal 1st order $(1\bar{1}01)$ plane, as well as activity on the prismatic 1st order $(1\bar{1}00)$ plane, beneath the indentation site. The stronger prismatic activity in the binary alloy at high inclination angles is consistent with the higher resolved stresses on c-component slip systems and aligns with the predicted reduction in γ_{USF} for $\langle c+a \rangle$ pyramidal systems in the ternary alloy.

Several regions in the TEM lamella, taken from the ternary alloy, reveal intersections between different 1st order prismatic and pyramidal planes, i.e., the $(1\bar{1}00)$ and $(1\bar{1}01)$ planes (see Fig. 5), indicating the occurrence of cross-slip between these systems during plastic deformation. This observation of cross-slip beneath the surface, goes hand in hand with the curved slip morphology presented in Figure A and Figure C, which can be correlated with multiple slip activation. Similar curved surface traces have previously been reported in cubic *C*15 $CaAl_2$ Laves phases, for specific orientations exhibiting comparable cross-slip behaviour [58]. This phenomenon implies the operation of dislocations with $\langle a \rangle$ Burgers vectors, which is consistent with the atomistic simulation results. The simulations demonstrate that $\langle a \rangle$ slip has a much lower energy barrier (by >30 %) than $\langle c+a \rangle$ slip. Additionally, activating a full $\langle a \rangle$ dislocation is more favourable energetically than activating partial dislocations, as indicated by the absence of a stable stacking fault state along the $\langle a \rangle$ slip path in the GSFE profile (see Figure S2).

Consistent with the GSFE profiles, no non-basal stacking faults were observed in the TEM lamellae, indicating the absence of low-energy metastable fault configurations under room-temperature deformation. Basal stacking faults are formed via the synchro-Shockley partial dislocations and are associated with relatively low stacking fault energies [59]. Previous experimental investigations have reported the formation of two distinct prismatic 1st order stacking fault structures in a *C*14 Nb-based Laves phase, as observed via atomic-resolution scanning transmission electron microscopy (STEM), following deformation at different temperatures [60]. Our previous atomistic simulations of *C*14 $MgZn_2$ and $CaMg_2$ using semi-empirical interatomic potentials suggested that forming more stable prismatic stacking fault structures requires significant atomic rearrangement and diffusion, which is only feasible at elevated temperatures [34]. Therefore, under the room-temperature conditions of the present study, the formation of prismatic stacking faults is presumably unfavourable, which explains their absence in the TEM observations.

Activation of $\langle c \rangle$ or $\langle c+a \rangle$ slip systems is essential for accommodating strain in the $\langle c \rangle$ direction. Among all simulated planes, the prismatic 2nd order plane is unique in that the $\langle c \rangle$ component slip exhibits a lower energy barrier than the corresponding pure $\langle a \rangle$ component slip, highlighting its unique role in facilitating c-axis deformation. In the pyramidal 2nd order plane, the energy difference between the $\langle c+a \rangle$ and $\langle a \rangle$ component slips is notably smaller than in the 1st order slip planes, particularly in the ternary composition. Significantly, slip events involving the $\langle c \rangle$ component demonstrate the most substantial reduction in energy barriers (approximately 4 to 9 %) in the ternary composition compared to the stoichiometric $CaMg_2$. This phenomenon suggests that $\langle c \rangle$-axis plasticity plays a more significant role in off-stoichiometric compositions, consistent with the experimentally observed higher activation frequency of 2nd order planes in the ternary *C*14 Laves phase. The enhanced ease of activating $\langle c \rangle$-type slip is also reflected in the macroscopic mechanical response, as compositions with greater deviations from stoichiometry exhibit lower hardness (and indentation modulus). This correlation indicates that the softening behaviour arises not only from lattice dilation due to Ca enrichment but also from the increased accessibility of non-basal $\langle c \rangle$ and $\langle c+a \rangle$ slip systems, which facilitate more isotropic plastic accommodation under load.

Further insights into dislocation structures and dynamics are required to develop a deeper understanding of non-basal plasticity in *C*14 Laves phases. A recent STEM study characterised non-basal dislocation core structures in a Nb-based *C*14 Laves phase, correlating the dissociation of $\langle c+a \rangle$ dislocations following high-temperature deformation to both long-range lattice order and short-range atomic configurations [60]. Nevertheless, the mechanisms of non-basal dislocation motion remain incompletely understood in *C*14 Laves phases, including the full $\langle a \rangle$ dislocation involved in cross-slip and the activation of $\langle c \rangle$ component dislocations. The role of solute atoms in either facilitating or impeding dislocation motion, cross-slip, and dissociation in binary and ternary off-stoichiometric compositions requires further investigation by combining nanomechanical testing and atomistic simulations. This will enable purposeful tuning not only of properties, but likely also dominant defects, such as $\langle a \rangle$, $\langle c \rangle$, or $\langle c+a \rangle$ dislocations and the formation of stacking faults. In addition to their activation and the associated changes in hardness and modulus, defect interactions may then also affect further properties and mechanism, like crack formation [25,58,61], and functional properties like hydrogen storage performance are also known to depend sensitively on Laves phase composition [1,62].

5. Conclusions

The effect of off-stoichiometric chemistry on the room-temperature mechanical properties of the hexagonal *C*14 Ca-Mg-Al Laves phase was systematically investigated through a combined atomistic modelling and experimental approach. Guided by simulation results, a composition predicted to exhibit a pronounced change in mechanical response, $Ca_{37}Mg_{61}Al_2$, was selected and further investigated using nanoindentation, chemical, and structural characterisation. Comparative assessment with the binary *C*14 $CaMg_2$ system enabled the evaluation of compositional effects beyond simple ternary addition. The principal findings are summarised as follows:

Mechanical properties

Both atomistic simulation and experimental measurements reveal a significant reduction in mechanical stiffness and hardness with compositional deviation. Specifically, the hardness decreased from 3.4 ± 0.2 GPa in the binary phase to 2.4 ± 0.3 GPa in the ternary alloy, while the indentation modulus decreased from 55.1 ± 3.0 GPa to 50.0 ± 1.9 GPa. Atomistic simulation results confirm that enrichment of the A-type atoms (Ca) induces this softening, whereas substitution by Al has a negligible effect.

Activation of slip systems

Nanoindentation slip plane analysis reveals a more balanced distribution of non-basal slip systems across the measured orientations for the $Ca_{37}Mg_{61}Al_2$ sample. GSFE calculations corroborate these observations, showing a greater decrease in energy barriers for pyramidal 1st order slip in the ternary phase than in the binary phase. Compared to the $Ca_{31}Mg_{69}$ sample, activation of the prismatic 1st order slip system has found to be decreased, while the pyramidal 2nd order slip system increased.

Dislocation activity

Transmission electron microscopy further corroborated these findings, showing parallel slip bands on both pyramidal and prismatic 1st order planes within the same deformation regions. This microstructural evidence confirms the activation of ⟨a⟩ dislocations and highlights the energetic favourability of full dislocation motion on non-basal slip planes. Overall, the combined atomistic simulation and experimental results demonstrate that off-stoichiometric modification, specifically Ca enrichment, leads to lattice dilation and promotes non-basal dislocation activity, providing a mechanistic pathway to tailor the plasticity of *C*14 Laves phases through controlled compositional tuning.

In summary, this study establishes a direct link between atomistic predictions and experimental observations in *C*14 Ca-Mg-Al Laves phases, demonstrating that controlled off-stoichiometry can effectively tailor mechanical response. These findings highlight compositional tuning as a powerful strategy to modulate plasticity in otherwise brittle Laves phases, bridging atomistic insights with experimental validation and offering a framework for property and defect design in these abundant intermetallics.

CRediT authorship contribution statement

Martina Freund: Writing – original draft, Visualization, Resources, Investigation, Formal analysis, Conceptualization. **Sang-Hyeok Lee:** Writing – review & editing, Investigation, Data curation. **Peter Koch:** Formal analysis. **Pei-Ling Sun:** Investigation. **Zhuocheng Xie:** Writing – review & editing, Formal analysis. **Sandra Korte-Kerzel:** Writing – review & editing, Supervision.

Declaration of competing interest

The authors declare that they have no known competing financial interests or personal relationships that could have appeared to influence the work reported in this paper.

Acknowledgements

The authors gratefully acknowledge financial support by the Deutsche Forschungsgemeinschaft (DFG) to all projects involved in this paper A05 and Z the SFB1394 Structural and Chemical atomic Complexity – From Defect Phase Diagrams to Material Properties, project ID 409476157. This project has received funding from the European Research Council (ERC) under the European Union's Horizon 2020 research and innovation programme (grant agreement No 852096 FunBlocks). The authors gratefully acknowledge the computing time provided to them at the NHR Center NHR4CES at RWTH Aachen University (project numbers p0021574 and p0020431). The data used in this publication was managed using the research data management platform Coscine with storage space granted by the Research Data Storage (RDS) of the DFG and Ministry of Culture and Science (MKW) of the State of North Rhine-Westphalia (DFG: INST222/1261-1 and MKW: 214-4.06.05.08 - 139057).

Supplementary materials

Supplementary material associated with this article can be found, in the online version, at doi:10.1016/j.actamat.2026.122134.

References

[1] F. Stein, A. Leineweber, Laves phases: a review of their functional and structural applications and an improved fundamental understanding of stability and properties, J. Mater. Sci. 56 (9) (2021) 5321–5427.
[2] J. Ragani, et al., High-temperature deformation of the γ-Mg17Al12 complex metallic alloy, Scr. Mater. 65 (3) (2011) 253–256.
[3] H. Mathur, V. Maier-Kiener, S. Korte-Kerzel, Deformation in the γ-Mg17Al12 phase at 25–278 °C, Acta Mater. 113 (2016) 221–229.
[4] H. Suzuki, Chemical interaction of solute atoms with dislocations, Sci. Rep. Res. Inst. Tohoku Univ. A 4 (1952) 455–463.
[5] L. Zhang, et al., Microstructures and mechanical properties of Mg–Al–Ca alloys affected by Ca/Al ratio, Mater. Sci. Eng.: A 636 (2015) 279–288.
[6] S. Amerioun, S.I. Simak, U. Häussermann, Laves-phase structural changes in the system CaAl2-x Mg x, Inorg. Chem. 42 (5) (2003) 1467–1474.
[7] D. Amberger, P. Eisenlohr, M. Göken, On the importance of a connected hard-phase skeleton for the creep resistance of Mg alloys, Acta Mater. 60 (5) (2012) 2277–2289.
[8] T. Rzychoń, Characterization of Mg-rich clusters in the C36 phase of the Mg–5Al–3Ca–0.7 Sr–0.2 Mn alloy, J. Alloys Compd. 598 (2014) 95–105.
[9] B. Backes, et al., Particle hardening in creep-resistant Mg-alloy MRI 230D probed by nanoindenting atomic force microscopy, Metall. Mater. Trans. A 40 (2009) 257–261.
[10] D. Amberger, P. Eisenlohr, M. Göken, Microstructural evolution during creep of Ca-containing AZ91, Mater. Sci. Eng.: A 510 (2009) 398–402.
[11] Y. Terada, et al., A thousandfold creep strengthening by Ca addition in die-cast AM50 magnesium alloy, Metall. Mater. Trans. A 35 (9) (2004) 3029–3032.
[12] W. Qudong, et al., Effects of Ca addition on the microstructure and mechanical properties of AZ91magnesium alloy, J. Mater. Sci. 36 (12) (2001) 3035–3040.
[13] T. Müller, et al., Gleitbanduntersuchungen während und nach verformung der intermetallischen verbindung MgZn2, Krist. Tech. 7 (11) (1972) 1249–1264.
[14] D. Hinz, P. Paufler, G. Schulze, Temperature change experiments during secondary creep of the intermetallic compound MgZn2, Phys. Status Solidi(b) 36 (2) (1969) 609–615.
[15] T. Müller, P. Paufler, Yield strength of the monocrystalline intermetallic compound MgZn2, Phys. Status Solidi(a) 40 (2) (1977) 471–477.
[16] U. Krämer, G. Schulze, Gittergeometrische betrachtung der plastischen verformung von Lavesphasen, Krist. Tech. 3 (3) (1968) 417–430.
[17] A. Von Keitz, G. Sauthoff, Laves phases for high temperatures—Part II: stability and mechanical properties, Intermetallics 10 (5) (2002) 497–510.
[18] P. Paufler, Early work on laves phases in East Germany, Intermetallics 19 (4) (2011) 599–612.
[19] J. Zhu, et al., Point defects in binary Laves phase alloys, Acta Mater. 47 (7) (1999) 2003–2018.
[20] D. Thoma, J. Perepezko, A geometric analysis of solubility ranges in laves phases, J. Alloys Compd. 224 (2) (1995) 330–341.
[21] M.F. Chisholm, S. Kumar, P. Hazzledine, Dislocations in complex materials, Science 307 (5710) (2005) 701–703.
[22] R. Berry, G. Raynor, The crystal chemistry of the laves phases, Acta Crystallogr. 6 (2) (1953) 178–186.
[23] F. Stein, M. Palm, G. Sauthoff, Structure and stability of Laves phases. Part I. Critical assessment of factors controlling Laves phase stability, Intermetallics 12 (7–9) (2004) 713–720.
[24] P. Paufler, Deformation-mechanism maps of the intermetallic compound MgZn2, Krist. Tech. 13 (5) (1978) 587–590.
[25] M. Freund, et al., Influence of chemical composition on the room temperature plasticity of C15 Ca-Al-Mg laves phases, Acta Mater. (2024) 276.
[26] N. Takata, et al., Nanoindentation study on solid solution softening of Fe-rich Fe2Nb laves phase by Ni in Fe–Nb–Ni ternary alloys, Intermetallics 70 (2016) 7–16.
[27] N. Takata, et al., Transmission electron microscopy of Fe2Nb laves phase with C14 structure in Fe-Nb-Ni alloys, MRS Online Proc. Libr. (OPL) (2008) 1128, 1128-U08-06.
[28] T. Takasugi, M. Yoshida, The effect of ternary addition on structure and stability of NbCr2 laves phases, J. Mater. Res. 13 (9) (1998) 2505–2513.
[29] T. Takasugi, M. Yoshida, S. Hanada, Deformability improvement in C15 NbCr2 intermetallics by addition of ternary elements, Acta Mater. 44 (2) (1996) 669–674.
[30] F. Chu, et al., Phase stability and defect structure of the C15 laves phase Nb (Cr, V) 2, Acta Mater. 46 (5) (1998) 1759–1769.
[31] N. Ulumuddin, S. Korte-Kerzel, Z. Xie, First-principles insights into the site occupancy of Ta–Fe–Al C14 laves phases, Comput. Mater. Sci. 253 (2025) 113856.
[32] Tehranchi, A., et al., Phase stability and defect studies of Mg-based laves phases using defect phase diagrams. arXiv preprint arXiv:2303.09576, 2023.
[33] Ladines, A.N., R. Drautz, and T. Hammerschmidt, Off-stoichiometric softening and polytypic transformations in the plastic deformation of the C14 Fe2Nb laves phase. arXiv preprint arXiv:2303.05553, 2023.
[34] Z. Xie, et al., On the temperature and composition dependence of non-basal stacking faults in C14 laves phases, Adv. Eng. Mater. 26 (20) (2024) 2400885.
[35] Z. Xie, et al., Unveiling the mechanisms of motion of synchro-shockley dislocations in laves phases, Phys. Rev. Mater. 7 (5) (2023) 053605.
[36] C. Zehnder, et al., Plastic deformation of single crystalline C14 Mg2Ca laves phase at room temperature, Mater. Sci. Eng.: A 759 (2019) 754–761.
[37] A.P. Thompson, et al., LAMMPS-a flexible simulation tool for particle-based materials modeling at the atomic, meso, and continuum scales, Comput. Phys. Commun. 271 (2022) 108171.

[38] I.S. Novikov, et al., The MLIP package: moment tensor potentials with MPI and active learning, Mach. Learn.: Sci. Technol. 2 (2) (2020) 025002.
[39] M. Poul, L. Huber, J. Neugebauer, Automated generation of structure datasets for machine learning potentials and alloys, npj Comput. Mater. 11 (1) (2025) 174.
[40] P. Hirel, Atomsk: a tool for manipulating and converting atomic data files, Comput. Phys. Commun. 197 (2015) 212–219.
[41] J. Guénolé, et al., Assessment and optimization of the fast inertial relaxation engine (fire) for energy minimization in atomistic simulations and its implementation in lammps, Comput. Mater. Sci. 175 (2020) 109584.
[42] A. Stukowski, Visualization and analysis of atomistic simulation data with OVITO–the Open Visualization Tool, Model. Simul. Mater. Sci. Eng. 18 (1) (2009) 015012.
[43] Luo, W., et al., Metallurgical synthesis methods for Mg-Al-Ca scientific model materials. arXiv preprint arXiv:2303.08523, 2023.
[44] W.C. Oliver, G.M. Pharr, An improved technique for determining hardness and elastic modulus using load and displacement sensing indentation experiments, J. Mater. Res. 7 (6) (1992) 1564–1583.
[45] W.C. Oliver, G.M. Pharr, Measurement of hardness and elastic modulus by instrumented indentation: advances in understanding and refinements to methodology, J. Mater. Res. 19 (1) (2004) 3–20.
[46] J.S.-L. Gibson, et al., Finding and characterising active slip systems: a short review and tutorial with automation tools, Materials 14 (2) (2021) 407.
[47] P. Hazzledine, P. Pirouz, Synchroshear transformations in laves phases, Scr. Metall. Mater. 28 (10) (1993) 1277–1282.
[48] P. Hazzledine, et al., Synchroshear of laves phases, MRS Online Proc. Libr. (OPL) (1992) 288.
[49] Z. Xie, et al., Thermally activated nature of synchro-shockley dislocations in laves phases, Scr. Mater. 235 (2023) 115588.
[50] S. Schröders, et al., Room temperature deformation in the Fe7Mo6 μ-phase, Int. J. Plast. 108 (2018) 125–143.
[51] M. Freund, et al., Plastic deformation of the CaMg2 C14-laves phase from 50 to 250 °C, Materialia 20 (2021) 101237.
[52] M. Freund, et al., Plasticity of the C15-CaAl2 laves phase at room temperature, Mater. Des. 225 (2023) 111504.
[53] K. Momma, F. Izumi, VESTA 3 for three-dimensional visualization of crystal, volumetric and morphology data, J. Appl. Crystallogr. 44 (6) (2011) 1272–1276.
[54] L. Shao, et al., The native point defects in C14 Mg2Ca laves phase: a first-principles study, Intermetallics 65 (2015) 29–34.
[55] C. Gasper, et al., Mechanical properties and deformation mechanisms of the C14 laves and μ-phase in the ternary Ta-Fe (-Al) system, Mater. Des. (2025) 113625.
[56] W. Luo, et al., Composition dependence of hardness and elastic modulus of the cubic and hexagonal NbCo2 laves phase polytypes studied by nanoindentation, J. Mater. Res. 35 (2) (2020) 185–195.
[57] M. Freund, et al., Redefining plasticity in a cubic intermetallic: dislocation dynamics in the CaAl2 laves phase, Acta Mater. (2025) 121604.
[58] J. Guénolé, et al., Basal slip in laves phases: the synchroshear dislocation, Scr. Mater. 166 (2019) 134–138.
[59] Y. Zhang, et al., Shuffle and glide mechanisms of prismatic dislocations in a hexagonal C 14-type laves-phase intermetallic compound, Phys. Rev. B 102 (13) (2020) 134117.
[60] Y. Zhang, L. Sheng, Dissociation and motion of< c+ a>dislocations in a C14 laves phase, Acta Mater. (2025) 121096.
[61] G. Liu, et al., On the atomic nature of complex dislocation locks in C15 laves phases, Acta Mater. (2025) 121700.
[62] K.-H. Young, S. Chang, X. Lin, C14 Laves phase metal hydride alloys for Ni/MH batteries applications, Batteries 3 (3) (2017) 27.